

## Laser-Focused Atomic Deposition

J. J. McClelland,\* R. E. Scholten, E. C. Palm, R. J. Celotta

The ability to fabricate nanometer-sized structures that are stable in air has the potential to contribute significantly to the advancement of new nanotechnologies and our understanding of nanoscale systems. Laser light can be used to control the motion of atoms on a nanoscopic scale. Chromium atoms were focused by a standing-wave laser field as they deposited onto a silicon substrate. The resulting nanostructure consisted of a series of narrow lines covering 0.4 millimeter by 1 millimeter. Atomic force microscopy measurements showed a line width of  $65 \pm 6$  nanometers, a spacing of 212.78 nanometers, and a height of  $34 \pm 10$  nanometers. The observed line widths and shapes are compared with the predictions of a semiclassical atom optical model.

Since the advent of microelectronics in the 1960s, there has been an increasing demand for smaller and faster electronic devices. Available technologies for the production of such devices on a commercial scale are reaching fundamental size limitations, and consequently, considerable research is now directed toward the development of fabrication techniques that will extend the current trends in device miniaturization. In optical lithography, feature size is limited, by diffraction, to approximately the wavelength of the light used, which with deep ultraviolet light approaches  $0.2 \mu\text{m}$ . The extension of such techniques to the x-ray region offers promise for the reduction of the minimum feature size (1) but is still in the development stage.

This work explores an inherently parallel approach to the fabrication of nanometer-size structures. With the use of the optical forces of near-resonant laser light on atomic beams, atoms are focused into subwavelength structures during deposition onto a substrate. Immediately above the substrate, an array of "atom lenses" formed by the laser light focuses the atoms into small areas to create the desired pattern. This approach has been investigated in experiments on focused deposition of sodium by Timp *et al.* (2). In contrast to a two-step lithographic process, in which a pattern is transferred to a surface by the patterning of a resist mask and etching of unmasked regions, this method directly deposits the desired nanostructure onto a surface.

Laser fields affect atomic trajectories through two types of force: the spontaneous force and the dipole or gradient force. The simplest spontaneous force arises when an atom repeatedly absorbs a photon from the laser field and then re-radiates a photon in a random direction through spontaneous emission. On average, there is a net transfer of momentum in the direction of the ab-

sorbed photons because the emitted-photon momenta average to zero. The spontaneous force can be used to heat or cool an ensemble of atoms, as applied in the field of laser cooling (3). From our perspective, this force is useful because it can be used to collimate an atomic beam without loss of flux (4).

With the dipole force, the atom, an oscillating dipole driven by the laser field, feels a force proportional to the intensity gradient in the oscillating electric field of the laser. The force is toward either high- or low-intensity regions, depending on whether the laser frequency is below (red detuning) or above (blue detuning) the natural atomic resonance frequency. In laser-focusing applications, the dependence of the dipole force on a gradient in the laser intensity allows variations in the intensity, such as those found in an interference pattern, to be used to form an atomic lens. Both the spontaneous and dipole forces depend on the laser intensity and the strength of coupling between the laser field and the atom. This coupling is ordinarily quite small, except when the laser frequency is close to an atomic resonance.

Chromium is a particularly good atom for the study of laser-focused deposition. The laser configuration required is within the range of current technology: Chromium has an optical transition from the ( ${}^7S_3$ ) ground state to the ( ${}^7P_4$ ) excited state at a vacuum wavelength of  $\lambda = 425.55 \text{ nm}$ . This transition, with a natural line width of  $\Gamma = 5 \text{ MHz}$ , is accessible with a single-frequency dye laser operating with a stilbene laser dye. No significant population traps exist; although there are some intermediate  ${}^5D$  levels, transitions to these states have low transition probabilities (about  $10^4 \text{ s}^{-1}$ ). Naturally occurring chromium is 84%  ${}^{52}\text{Cr}$ , which has no hyperfine structure, and so a majority of the atoms are all focused identically. In addition, chromium is a self-passivating metallic material that has a very low mobility on most surfaces. Thus, the fabricated structures are expected to

have good stability after they are deposited, even if removed from vacuum.

As the first step in the exploration of laser-focused deposition, we deposited chromium atoms onto a silicon substrate using a one-dimensional standing wave (Fig. 1). The intensity variations within the standing wave create a series of parallel dipole-force potential wells, spaced  $\lambda/2$  apart, aligned perpendicular to the atom beam. For blue detunings (laser frequency above the atomic resonance), the potential minima lie along the standing wave nodes. The atoms experience a force toward these potential minima and are therefore focused into a series of lines.

The experimental arrangement is shown in Fig. 2. A beam of chromium atoms is produced by a high-temperature effusion source operating at  $1575^\circ\text{C}$ . The atom beam is collimated with an aperture followed by a region of transverse laser cooling. Collimation of the atom beam is necessary before focusing because the depth of the standing wave potential wells is very small compared with the transverse thermal kinetic energy of the chromium atoms. Only those atoms that have a kinetic energy transverse to the beam of less than the potential depth will be focused, whereas those with greater transverse energies will skip across wells. The transverse kinetic energy depends on the divergence angle of the beam, which must typically be a fraction of a milliradian.

This degree of collimation is readily obtained with the use of spontaneous forces to transversely cool the atom beam. Two counter-propagating laser beams intersect the atom beam at right angles to generate what is sometimes referred to as "optical molasses" (5). The laser beams, which come from the same laser as the standing wave beam, are frequency shifted with an acousto-optic modulator to slightly below the atomic resonance frequency. Through interactions with these laser beams, the atoms experience Doppler and polarization gradient cooling, which together reduce the transverse-velocity spread to below the Doppler limit (6).

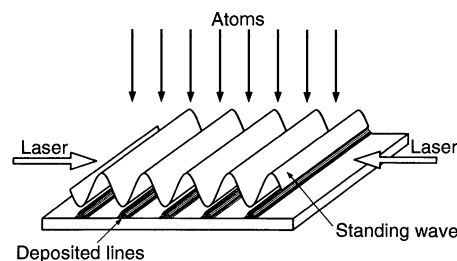


**Fig. 1.** A standing wave laser field forms a series of cylindrical lenses for chromium atoms, focusing them into nanometer-sized lines as they deposit onto a substrate.

Electron Physics Group, National Institute of Standards and Technology, Gaithersburg, MD 20899.

\*To whom correspondence should be addressed.

We measured the residual divergence of the atom beam by removing the deposition substrate and standing wave and allowing the atoms to travel freely over a distance of up to 750 mm. A probe laser beam illuminated the atoms after their free flight, and an image of the fluorescence was collected on a charge-coupled device (CCD) camera. Residual divergence angles of less than 0.2 mrad [full width at half maximum (FWHM)] were measured with  $12 \pm 2$  mW (7) of laser power in each cooling beam (Fig. 3). For comparison, similar collimation could be achieved without laser cooling, with a 1-mm slit separated from the oven by 5 m, but with a 92% loss in flux.

For the deposition of chromium lines, the silicon sample was mounted, facing the atomic beam, on a glass-ceramic plate with a low thermal expansion coefficient. A small mirror was mounted directly against the edge of the plate, perpendicular to the silicon surface, to provide the reflection required to create the standing wave. Mounting the mirror against the glass-ceramic plate was critical because the mirror surface determines the locations of the nodes of the standing wave. Any mechanical or thermal motion of the silicon relative to the mirror surface, on the scale of nanometers, would result in a blurring of the deposited lines.

The standing wave was formed with a nominally Gaussian, circularly polarized laser beam focused such that its waist location coincided with the standing wave mirror. The substrate position was adjusted to occlude half the standing wave, such that the standing wave beam grazed along the substrate surface with a half-Gaussian intensity profile whose maximum was at the surface. We minimized deviations from the half-Gaussian profile, resulting from diffraction

and reflection at the silicon surface, by keeping the substrate small, the distance between the substrate and the standing wave mirror short, and by making the standing wave mirror perpendicular to the silicon surface within 0.5 mrad. Because of the small potential depth of the standing wave compared with the longitudinal kinetic energy of the atoms, it was also necessary to ensure that the standing wave was perpendicular to the collimated atom beam within a fraction of a milliradian.

After each deposition, the samples were removed from the vacuum system and examined by scanning electron microscopy (SEM) and atomic force microscopy (AFM). Well-defined lines were observed (Fig. 4), with uniform shape and spacing extending over the full area covered by the standing wave laser beam, despite its Gaussian profile. The deposition rate of atoms from the chromium source was  $0.7 \pm 0.2$  nm per minute, as determined with a quartz crystal microbalance, and the samples were exposed for a total of 20 min, giving an average chromium thickness of  $14 \pm 4$  nm.

The line profile (Fig. 5) of Fig. 4 is an average of AFM data along the chromium lines, covering a distance of  $0.5 \mu\text{m}$ . The average FWHM of the peaks in this line scan is  $66 \pm 1$  nm, and the height is  $34 \pm 10$  nm. The peaks all had quite uniform height in the profile; the uncertainty in the height results from the systematic uncertainty in the AFM calibration. From this and other line scans taken from samples prepared under similar conditions, we obtained an average width of 65 nm, with a standard deviation of 6 nm. The variation in the widths is believed to be a result of systematic variations in both the transverse laser cooling and the AFM imaging process, both of which have a significant effect on

the observed line width of the structures.

To better understand the focusing of atoms onto a substrate with a standing wave laser beam, we modeled the process with a semiclassical approach. The motion of the atoms is treated as a series of classical trajectories traced on a potential surface derived from a quantum treatment of the dipole force.

The potential associated with the dipole force can be written as (8)

$$U = \frac{\hbar\Delta}{2} \ln(1+p) \quad (1)$$

where  $\hbar$  is Planck's constant divided by  $2\pi$ ,  $\Delta$  is the detuning of the laser from the atomic resonance frequency, and  $p$  is the saturation parameter, given by

$$p = \frac{I}{I_0} \frac{\Gamma^2}{\Gamma^2 + 4\Delta^2} \quad (2)$$

where  $I$  is the laser intensity,  $I_0$  is the atomic saturation intensity, and  $\Gamma$  is the natural atomic resonance line width. In the standing wave,  $I$  is proportional to  $\sin^2(2\pi x/\lambda)$ , where  $\lambda$  is the wavelength of the laser light, and  $x$  is the position along the standing wave.

Letting  $U$  represent the potential, we calculated a series of atom trajectories (Fig. 6). Some trajectories were traced assuming a perfectly collimated atom beam with no longitudinal velocity spread (Fig. 6A). In this case, the standing wave field functions quite well as a lens. With the right choice of laser intensity, profile, and detuning, an extremely sharp focus is attainable. The

**Fig. 2.** Schematic of the experiment, showing dye laser, vacuum system, chromium atomic beam, transverse laser cooling, standing wave, and sample holder. The atoms are collimated in the transverse laser cooling region before they are focused by the standing wave. The dye-laser frequency is set above the atomic resonance by 60 to 240 MHz. The laser cooling beams are frequency shifted with an acousto-optic modulator (AOM) to just below the atomic resonance. The laser cooling beams are linearly polarized perpendicular to each other by a quarter-wave retarder ( $\lambda/4$ ). A second quarter-wave retarder circularly polarizes the standing wave beam.

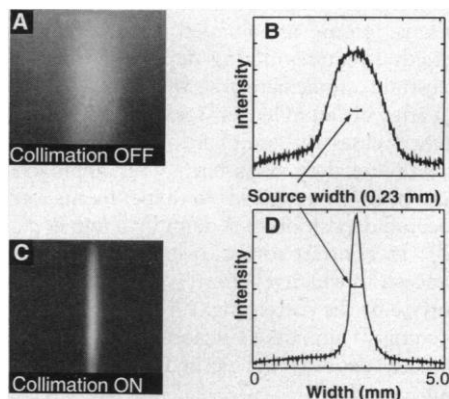
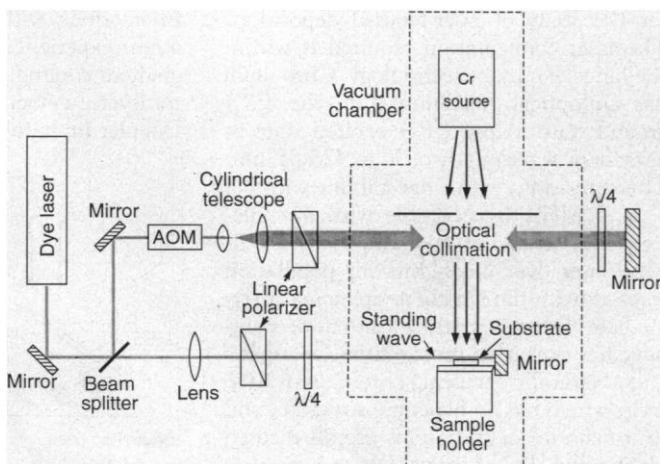


**Fig. 3.** Collimation of the chromium atomic beam with transverse laser cooling. The images, produced by laser-induced fluorescence, show the width of the atomic beam. The atom beam, traveling from top to bottom in the images, is precollimated with a 0.23-mm slit. (A) Image of the atom beam 410 mm downstream from the laser cooling region with collimation off, showing the normal divergence of the atoms. (B) Line scan of image shown in (A). (C) Image and (D) line scan with the collimation turned on, showing almost negligible spreading of the atom beam after it has traversed a distance of 410 mm.

width in Fig. 6A, which is 0.9 nm (FWHM), is attributable only to spherical aberration, that is, trajectories entering the lens far from its center do not reach the same focal point as those entering close to the center (9).

Because the trajectories are calculated classically, the resulting line width does not show any broadening attributable to the wave nature of the atoms. In fact, the line width is limited by diffraction, just as the minimum spot size of a lens in ordinary optics is diffraction-limited. In optics, the diffraction-limited line width (FWHM) for a cylindrical lens is given by  $w = 0.88\lambda/\alpha$ ,

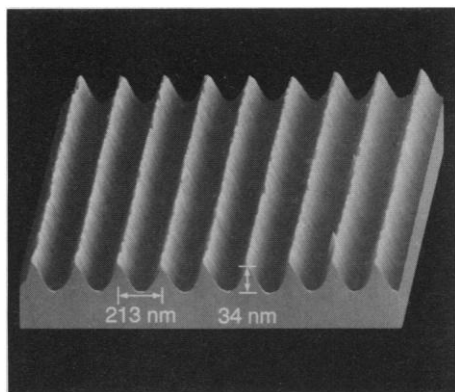


**Fig. 4.** A typical AFM image of chromium lines created by laser-focused atomic deposition. The image shows a  $2\ \mu\text{m}$  by  $2\ \mu\text{m}$  region of the lines, which cover a  $0.4\ \text{mm}$  by  $1\ \text{mm}$  area of the substrate. The sample was fabricated with an incident laser power of  $20 \pm 2\ \text{mW}$  in the incoming standing wave beam and a blue detuning of  $198 \pm 2\ \text{MHz}$ . The laser beam profile was approximately Gaussian with some ellipticity. The  $1/e^2$  full widths were  $0.39 \pm 0.02\ \text{mm}$  perpendicular to the silicon surface and  $0.47 \pm 0.02\ \text{mm}$  parallel to the surface.

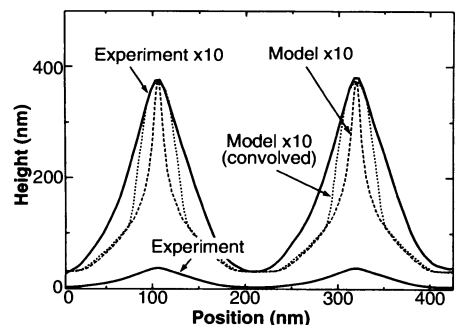


**Fig. 5.** Line scan of the AFM image in Fig. 4, compared with the shape predicted by model calculations. The experimental data is an average of AFM data along the chromium lines, covering a distance of  $0.5\ \mu\text{m}$ . The spacing, determined solely by the laser wavelength, is  $212.78\ \text{nm}$ , and the average peak width is  $66 \pm 1\ \text{nm}$ . The theoretical model prediction is based on the trajectory calculations shown in Fig. 6. Also shown is a convolution of the model prediction with a nominal AFM tip function.

where  $\alpha$  is the convergence angle at the focus (10). Replacing  $\lambda$  with the de Broglie wavelength  $\lambda_{\text{dB}}$  and obtaining  $\alpha$  from trajectory calculations, we can estimate this contribution to the line width in our atom lens. For the conditions of Fig. 6A,  $\lambda_{\text{dB}} = 0.008\ \text{nm}$ , and the resulting  $w$  is about  $9\ \text{nm}$ , 10 times larger than the contribution from spherical aberration.

In the experiments described here, the atoms are not completely collimated, they have a broad thermal velocity spread, and their population is distributed among a number of magnetic sublevels, each with its own value of  $I_0$ . We traced 140,000 trajectories (Fig. 6B) with a uniform distribution of  $x$  positions, a distribution of angles derived from measurements of the atom beam collimation, a Maxwell-Boltzmann distribution of velocities based on the chromium-source temperature, and a uniform distribution of magnetic sublevel populations.

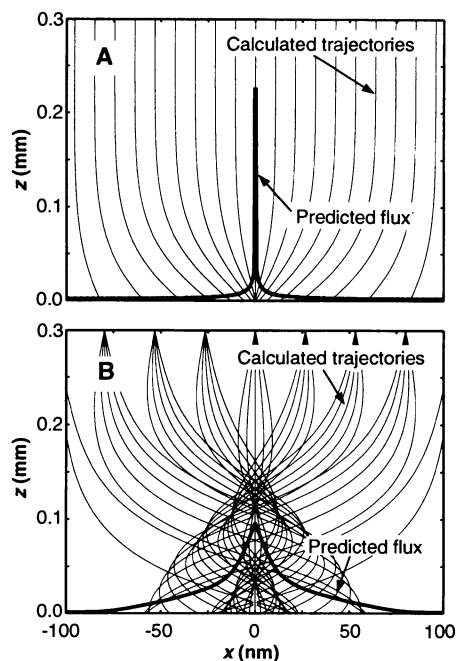


**Fig. 6.** Trajectory calculations of chromium atoms for one period of the standing wave laser field ( $212.78\ \text{nm}$ ), showing sample trajectories and the predicted flux at the sample. **(A)** Ideal situation in which the atom beam has a zero divergence angle and all the atoms have the same velocity of  $926\ \text{m/s}$  (the average thermal velocity of the chromium atoms as they emerge from the oven at a temperature of  $1500^\circ\text{C}$ ). The laser power,  $1/e^2$  diameter, and detuning are  $5.2\ \text{mW}$ ,  $0.39\ \text{mm}$ , and  $200\ \text{MHz}$ , respectively. **(B)** A more realistic calculation, corresponding to the deposition shown in Fig. 4. The atoms are given an angular distribution with FWHM of  $0.2\ \text{mrad}$  and a Maxwell-Boltzmann distribution in velocities based on the temperature of the oven. The laser intensity,  $1/e^2$  beam diameter, and detuning are  $20\ \text{mW}$ ,  $0.39\ \text{mm}$ , and  $200\ \text{MHz}$ , respectively. We determined the predicted flux by tracing 140,000 trajectories.

In this case, no clear focal point is discerned; rather, the atoms are “channeled” down the potential wells of the standing wave. As long as the laser intensity is present right up to the substrate, the atoms are still concentrated at the standing wave minima, so a concentration of atoms into lines is still seen. Interestingly, in this channeling mode, the predicted line widths are rather insensitive to laser power and beam profile.

A significant difference exists between the line shape of the model prediction and the experimental result (Fig. 5). This could be attributed to a number of factors, including effects of the AFM tip profile, omissions in the semiclassical theory, and possible surface diffusion of the chromium atoms after they land.

To roughly estimate the effect of the AFM tip on the measured line profile, we convolved the model prediction with a nominal tip function consisting of a  $70^\circ$  cone with a  $10\ \text{nm}$  radius on the point (11). The convolution broadens the theoretical line significantly, bringing it closer to agreement with the experiment (Fig. 5). This convolution indicates that the lines are likely to be narrower than the AFM measurements indicated; however, the uncertainty in our knowledge of the tip shape prevents us from drawing further conclusions about the true line width.

The model calculations omit several effects. Diffraction of the atoms is neglected because its contribution to the line width, when added in quadrature, is expected to be at most only  $2\ \text{nm}$ . Nonequilibrium and spontaneous-emission effects are also neglected. On average, the atoms spend about six natural lifetimes in the laser field, which is long enough for equilibrium between the atom and the laser field to be reached, yet short enough to limit the randomizing effects of spontaneous emission.

Our experiments demonstrate that atom optical techniques can be used to create, in parallel, a well-ordered array of nanometer-scale lines covering a macroscopic area. However, the true utility of these methods will become apparent when arbitrary patterns can be produced. The next step will be the construction of a two-dimensional standing wave, which will allow an array of identical dots to be deposited, separated by  $\lambda/2$  in each direction. If the substrate is scanned during deposition, each unit cell of the array will contain an identically “painted” pattern, with over  $2 \times 10^9$  such patterns per square centimeter, created in only a few minutes.

## REFERENCES AND NOTES

1. D. L. White *et al.*, *Solid State Technol.* **34**, 38 (July 1991).
2. G. Timp *et al.*, *Phys. Rev. Lett.* **69**, 1636 (1992).

- See also M. Prentiss, G. Timp, N. Bigelow, R. E. Behringer, J. E. Cunningham, *Appl. Phys. Lett.* **60**, 1027 (1992).
- See special issues "The Mechanical Effects of Light," *J. Opt. Soc. Am. B* **2**, 1706-1860 (1985) and "Laser Cooling and Trapping of Atoms," *ibid.* **6**, 2020-2226 (1989).
  - V. I. Balykin, V. S. Letokhov, A. I. Sidorov, *JETP Lett.* **40**, 1026 (1985); B. Sheehy, S.-Q. Shang, R. Watts, S. Hatamian, H. Metcalf, *J. Opt. Soc. Am. B* **6**, 2165 (1989).
  - S. Chu, L. Holberg, J. E. Bjorkholm, A. Cable, A. Ashkin, *Phys. Rev. Lett.* **55**, 48 (1985); P. D. Lett *et al.*, *J. Opt. Soc. Am. B* **6**, 2084 (1989).
  - C. N. Cohen-Tannoudji and W. D. Phillips, *Phys. Today* **43**, 33 (October 1990).
  - Uncertainty estimates are one standard deviation combined random and systematic uncertainties unless otherwise indicated.
  - J. P. Gordon and A. Ashkin, *Phys. Rev. A* **21**, 1606

- (1980); J. Dalibard and C. Cohen-Tannoudji, *J. Opt. Soc. Am. B* **2**, 1707 (1985).
- An analytical treatment of spherical aberration for laser focusing of atoms is given in J. J. McClelland and M. R. Scheinfein, *J. Opt. Soc. Am. B* **8**, 1974 (1991).
- See, for example, E. Hecht, *Optics* (Addison-Wesley, Reading, MA, ed. 2, 1987).
- Nominal AFM tip dimensions were taken from manufacturer specifications.
- We thank J. Fu for assistance in obtaining AFM images and A. Gavrin for assistance with preliminary SEM studies of our samples. Supported in part by the Technology Administration of the U.S. Department of Commerce and by the Division of Chemical Sciences, Office of Basic Energy Sciences, Office of Energy Research, U.S. Department of Energy.

14 July 1993, accepted 23 September 1993

## Carbon-Free Fullerenes: Condensed and Stuffed Anionic Examples in Indium Systems

Slavi C. Sevov and John D. Corbett\*

Condensed, well-ordered analogs of the fullerenes occur in the hexagonal phases  $\text{Na}_{96}\text{In}_{97}\text{Z}_2$  ( $Z = \text{nickel, palladium, or platinum}$ ). Large cages of  $\text{In}_{74}$  ( $D_{3h}$ ) and  $\text{M}_{60}$  ( $= \text{In}_{48}\text{Na}_{12}, D_{3d}$ ) share pentagonal faces to generate a double-hexagonal close-packed analog of NiAs. All these polyhedra are centered by partially disordered  $\text{In}_{10}\text{Z}$  clusters within deltahedra of sodium atoms that cap all inner faces of the cages, namely,  $\text{Z}@_{\text{In}_{10}}@_{\text{Na}_{39}}@_{\text{In}_{74}}$  and  $\text{Z}@_{\text{In}_{10}}@_{\text{Na}_{32}}@_{\text{Na}_{12}}@_{\text{In}_{48}}$  "onions." The highest filled bands in these compounds apparently involve localized electron pairs on surface features on  $\text{In}_{74}$ -based layers. Structural and electronic relations between diamond and NaIn (stuffed diamond structure) parallel those between certain fullerenes and  $\text{Na}_{96}\text{In}_{97}\text{Z}_2$  and, presumably, other valence-driven intermetallic phases.

The fullerenes  $\text{C}_{60}$ ,  $\text{C}_{70}$ , and their derivatives that are generating so much interest and so many novel results (1, 2) naturally raise the question of whether similar "naked" cage species might be synthesized for other main-group elements. The strong  $\pi$  bonds formed by C must be a major factor in the kinetic stabilities of the fullerenes, whereas the possibility of heavier element analogs may be limited by the ease with which they rearrange to other more stable structures. Analogous ions naturally have different decomposition reactions (3). Important examples are the original Zintl phases NaTl, NaIn, and Li(Al,Ga,In) where the presumed anionic group-13 elements form a diamond lattice that is stuffed with the cations (4, 5). Recent studies indicate that Zintl's very simple isolectronic analogy seems to have merit (6).

We report a remarkable alternative in In chemistry, fulleride-like species such as  $\text{In}_{74}$  that share pentagonal faces to form layers and are also stuffed with both centered  $\text{In}_{10}\text{Ni}^{10-}$ -like clusters and Na deltahedra that screen the

clusters from the In cages. One principal array would be described as  $\text{Ni}@_{\text{In}_{10}}@_{\text{Na}_{39}}@_{\text{In}_{74}}$  in the nomenclature of Smalley and co-workers (1, 7). Size proportions appear to be particularly important because substitution of either K or Ga for Na or In affords nothing comparable. Two series have been discovered: hexagonal  $\text{Na}_{96}\text{In}_{97}\text{Z}_2$  (1) and orthorhombic  $\text{Na}_{172}\text{In}_{197}\text{Z}_2$  (2), where Z may be Ni, Pd, or Pt (8). Members of both groups afford well-refined, single-crystal x-ray definition of nearly all aspects of the structures to reveal  $\text{In}_{70}$ ,  $\text{In}_{74}$ , and  $\text{In}_{78}$  fullerene-like cages as well as distinct  $\text{M}_{60} = \text{In}_{48}\text{Na}_{12}$  polyhedra. These are in notable contrast to the rotationally disordered fullerene and fulleride solids for which characterization has relied heavily on nuclear magnetic resonance. The structure of 1 with Ni and Pd will be reported here (9, 10) together with a few relevant aspects of 2 containing Ni. The latter will be described elsewhere because of its 141 independent atoms and structural complexity (11).

The novel phases  $\text{Na}_{96}\text{In}_{97}\text{Z}_2$  exhibit several features of note. The  $\text{In}_{74}$  cages of  $D_{3h}$  ( $6m2$ ) symmetry (Fig. 1) have In-In distances of 2.92 to 3.05 Å, typical for delocalized bonding in smaller clusters  $\text{In}_n$ , where  $n = 11, 12, \text{ or } 16$  (12-17). The

deployment of these and other unusual features in the cell is generalized in Fig. 2. All three-bonded In atoms gain at least one additional In neighbor, presumably to compensate for the absence of the good  $\pi$  bonding. Of the 12 pentagonal faces customary in fullerenes, the six in  $\text{In}_{74}$  about the horizontal mirror plane ( $\text{In}_{2, 4, 7, 7, 4}$ ; Fig. 1) are shared with like cages to generate close-packed layers. Five such pentagons are shaded in Fig. 2. Each polyhedron has a diameter of 16.0 Å (the  $a$  axis) about the waist and 15.5 Å along the  $c$  axis versus  $\sim 7.1$  Å for  $\text{C}_{60}$ . Space is filled with three additional features: (i) small surface units of In that augment bonding of atoms in  $\text{In}_{74}$  where intercage In-In interactions are not possible; (ii) specifically ordered and roughly spherical shells of endo- and exohedral Na on all cages; and (iii) seemingly identical cluster anions  $\text{In}_{10}\text{Z}$  within both  $\text{In}_{74}$  (A) and in an interlayer region defined by  $\text{M}_{60} = \text{In}_{48}\text{Na}_{12}$  (B) (see below). Inappropriate spatial and symmetry constraints provided by the (nonbonded)  $\text{Na}_{39}$  and  $\text{Na}_{32}$  polyhedra, which line the respective polyhedra, appear to preclude well-ordered  $\text{In}_{10}$  units about the central Z. All other atoms in both the Ni and Pd compounds refined well.

Each of these three features will be described separately. First, additional inter-cage bonds form between like In5 and In6 atoms that adjoin the shared pentagons (Fig. 1), In5 in triangles between three  $\text{In}_{74}$  and, at higher latitude, In6 in pairs [figure in (10)]. Two decorations or "warts" fill out the remaining In bonding on the cage surfaces and, with Na and  $\text{In}_{10}\text{Ni}$  (B), separate the layers. As seen near the middle of Fig. 2, triangles of In11 cap the polar In9 and bond to three neighboring In8, and hexagons of In10 sit above the interstices

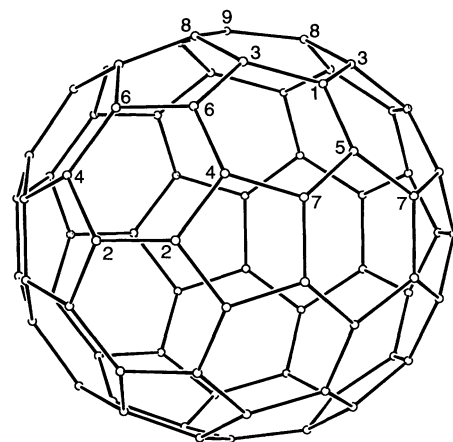


**Fig. 1.** The  $\text{In}_{74}$  fullerene, which shares pentagons about the waist to generate close-packed layers. The point symmetry is  $D_{3h}$ , with the  $c$  axis vertical through the polar In9 atoms (30% probability ellipsoids).

Ames Laboratory and Department of Chemistry, Iowa State University, Ames, IA 50011.

\*To whom correspondence should be addressed.